Renewable Energy 264 (2026) 125555

Contents lists available at ScienceDirect

Renewable Energy

journal homepage: www.elsevier.com/locate/renene

Cascading valorization of *Miscanthus* biomass for bioethanol, lactic acid and nanomaterials via green-like pretreatment with reusable fertilizers

Bing Gao [a], Junsheng Yu [a], Ling Luo [a], Lei Zhu [a], Zongtai Tang [a], Yongtai Wang [a], Jiacheng Kang [a], Dan Sun [b], Hao Peng [a], Yanting Wang [a], Liangcai Peng [a,c], Hua Yu [a,*]

[a] Key Laboratory of Fermentation Engineering (Ministry of Education), Hubei Key Laboratory of Industrial Microbiology, National "111" Center for Cellular Regulation & Molecular Pharmaceutics, Biomass & Bioenergy Research Center, School of Life & Health Sciences, Hubei University of Technology, Wuhan, 430068, China
[b] School of Material Science & Chemical Engineering, Hubei University of Technology, Wuhan, 430068, China
[c] College of Plant Science & Technology, Huazhong Agricultural University, Wuhan, 430070, China

ARTICLE INFO

Keywords:
Miscanthus
Green-like technology
Enzymatic hydrolysis
Bioproducts
Biomass valorization

ABSTRACT

Miscanthus provides diverse lignocellulose substrates convertible for sustainable biofuels and valuable bioproducts. Due to lignocellulose recalcitrance, however, a cost-effective and environmentally friendly strategy is required for biomass valorization with minimal biomass loss. In this study, a green-like pretreatment was initially explored for two distinct *Miscanthus* accessions (*M. lutarioriparius*/Mlu10 and *M. sacchariflorus*/Msa21) using crop-reusable fertilizers (K_3PO_4, K_2CO_3). Under the optimal pretreatment (10% K_3PO_4, 2.5 h), the *Miscanthus* showed a maximum lignin removal at 67% for a remarkably increased lignocellulose porosity by 2.6-4.5 folds. These structural improvements significantly enhanced biomass enzymatic saccharification accountable for 81% cellulose conversion into hexose (14.39 g/L), which subsequently improved both yeast and bacterial fermentations for yielding 28% bioethanol (7.81 g/L) and 68% lactic acid (20.19 g/L) on the basis of cellulose mass. Furthermore, the enzyme-undigested lignocellulose residues were employed to produce cellulose nanofibers (CNFs), whereas the pretreatment supernatants were utilized to generate lignin nanoparticles (LNPs). Notably, the CNFs and LNPs were fully integrated by Tween-80 for desirable biosorbents assembly, which showed significantly upgraded adsorption with a maximum Langmuir capacity of 59.52 mg/g for methylene blue. Mass balance analysis indicated that Msa21 is optimal for sugar-based bioconversion, whereas Mlu10 is favor for material-oriented valorization. Therefore, this study demonstrates a green-like strategy that efficiently produces bioethanol and lactic acid and effectively generates functional biosorbents from distinct *Miscanthus* accessions and beyond.

1. Introduction

Miscanthus spp. has emerged as a highly promising feedstock for renewable energy and bio-based materials owing to its high biomass yield, exceptional photosynthetic efficiency, and broad environmental adaptability [1,2]. Its rapid growth cycle and strong carbon sequestration capacity make it a sustainable source for bioethanol production, thermochemical conversion, and other clean energy applications [3,4]. In addition, its well-developed root system and remarkable stress tolerance enable applications in soil remediation and ecological restoration [5,6]. These attributes collectively position *Miscanthus* as an ideal model for constructing an integrated biorefinery platform, which aims to convert lignocellulosic biomass into a spectrum of value-added products including bioethanol, biochemicals and bioproducts as a simultaneously promoted sustainability [7,8].

Nevertheless, the intrinsic recalcitrance of lignocellulosic biomass—arising from the compact, cross-linked network of cellulose, hemicellulose, and lignin—severely restricts enzymatic accessibility and catalytic efficiency [9,10]. Effective pretreatment is therefore essential to overcome these structural barriers and unlock the full bioconversion potential of *Miscanthus* [11,12]. Among various methods [13,14], alkaline pretreatment (e.g., NaOH, K_3PO_4, $NaCO_3$) [15] is widely adopted for its efficient delignification and cellulose preservation [16]. To promote greener and more sustainable processes, environmentally friendly alkaline salts such as potassium phosphate (K_3PO_4) and potassium carbonate (K_2CO_3) have gained increasing attention [17]. These

* Corresponding author.http://bbrc.hbut.edu.cn
E-mail address: yh201906@foxmail.com (H. Yu).

https://doi.org/10.1016/j.renene.2026.125555
Received 7 October 2025; Received in revised form 20 January 2026; Accepted 4 March 2026
Available online 7 March 2026

salts not only provide moderate alkalinity and strong delignification efficiency [18], but also enable potassium recovery and reuse as agricultural fertilizers, aligning with circular economy principle [19].

Despite significant progress in pretreatment technologies, most biorefineries still operate under a linear utilization model [20], which results in incomplete resource valorization. Enzymatic hydrolysis residues, typically enriched in crystalline cellulose [21], and lignin solubilized in pretreatment liquors are often treated as waste streams [22], with their functional potential largely underestimated [23]. In particular, lignin's unique aromatic backbone and abundant functional groups render it a promising precursor for advanced functional materials [24]. Moving beyond the traditional linear paradigm [25], the integration of lignin nanoparticles (LNPs) with cellulose nanofibers (CNFs) via green crosslinking strategies provides a sustainable route to fabricate high-performance composites with hierarchical porous structures [26], thereby extending the biomass value chain and advancing holistic biorefinery development.

In this context, the present study aims to establish a closed-loop biorefinery paradigm for the full-component valorization of *Miscanthus* [27]. By selecting two representative *Miscanthus* (Mlu10 and Msa21) accessions, this study systematically evaluated the green-like pretreatments using K_3PO_4 and K_2CO_3 at 121 °C (0.1 MPa) for 2.5 h, and then determined biomass enzymatic saccharification and fermentation performances toward bioethanol and lactic acid production. [28,29]. A key innovation of this work lies in the downstream valorization of pretreatment by-products: lignin nanoparticles recovered from the pretreatment liquor were co-assembled with cellulose nanofibers from enzymatic residues to fabricate a high-performance bio-based adsorbent [30]. This strategy not only enhances the yields of primary bioproducts (biofuels and platform chemicals) but also transforms by-products into value-added materials, providing a novel theoretical framework and practical approach for high-value utilization of lignocellulosic biomass with less residue release [31].

2. Materials and methods

2.1. Collection of biomass samples

Four types of *Miscanthus* (Mlu10, Msa21, Msa22, and Msa32) were selected from the *Miscanthus* resource bank and cultivated under uniform agronomic conditions in the experimental field of Huazhong Agricultural University (Wuhan, China). All mature plant tissues were collected, and their leaves and branches were removed. The stems were dried at 60 °C, and ground using a crusher (QE-300) [32]. The ground powder was sieved through a 40-mesh sieve (0.425 mm × 0.425 mm) and then placed in an oven at 60 °C for dehydration to constant weight before storage.

2.2. Determination of cell wall components

Cell wall polysaccharides were sequentially extracted following the stepwise fractionation method described by Refs. [33,34],allowing the separation of soluble sugars, pectin, hemicellulose, and cellulose fractions. Hexose and pentose contents were quantified using a UV–visible spectrophotometer (V-1100D; Shanghai Mapada Instruments Co., Ltd.). For cellulose determination, samples were hydrolyzed with 67% (v/v) H_2SO_4, and hexose content was quantified by the anthrone–H_2SO_4 colorimetric method. Hemicellulose content was calculated as the sum of hexoses and pentoses present in the hemicellulose fraction. The total lignin (acid soluble/insoluble) content was determined using a two-step H_2SO_4 hydrolysis method according to the Laboratory Analytical Procedure of the National Renewable Energy Laboratory (NREL) [35]. All measurements were performed in triplicate with independent biological replicates to ensure reproducibility.

2.3. Determination of lignin monomer content and total phenolic content

Lignin monomers were extracted by the nitrobenzene oxidation method, authentic standards of H-, G-, and S-type lignin monomers were obtained from Sinopharm Chemical Reagent Co., Ltd. Quantitative analysis was performed on a Shimadzu LC-20A high-performance liquid chromatography (HPLC) system equipped with a UV detector set at 280 nm, using a Kromat Universal C18 column (4.6 mm × 250 mm, 5 μm). The mobile phase consisted of methanol:water: acetic acid (16:63:1, v/v/v) at a flow rate of 1.1 mL/min, with an injection volume of 20 μL. Each measurement was conducted in triplicate using independent biological replicates to ensure accuracy and reproducibility.

The total phenolic content (TPC) of lignin released into the pretreatment supernatant was determined using the Folin–Ciocalteu colorimetric assay with slight modifications [36]. Briefly, 1.0 mL of appropriately diluted sample solution was mixed with 5.0 mL of 10% (v/v) Folin–Ciocalteu reagent. After incubation for 5 min at room temperature, 4.0 mL of 7.5% (w/v) sodium carbonate solution was added, followed by thorough mixing. The reaction mixture was incubated at 40 °C for 30 min in the dark, and the absorbance was measured at 760 nm using a UV–Vis spectrophotometer. Gallic acid was used as an external standard to generate a calibration curve (0–200 mg/L), and results were expressed as gallic acid equivalents (GAE, mg GAE/L). All measurements were performed in triplicate.

2.4. Material pretreatment and enzymatic hydrolysis

2.4.1. Material pretreatment

Miscanthus powder was separately mixed with 10% (w/w) K_3PO_4 and 10% (w/w) K_2CO_3 (each at a solid-to-liquid ratio of 1:10), and each mixture was reacted in a high-pressure steam sterilizer at 121 °C for 2.0-3.5 h. Subsequently, the mixture was transferred into a 50 mL centrifuge tube and centrifuged at 3000 g for 5 min. The supernatants were collected for lignin recovery, while the residues were washed once with 6 mL of phosphate buffer solution (pH 4.8) prior to enzymatic hydrolysis.

2.4.2. Enzymatic hydrolysis

The residue was added to a 2.0 g/L cellulase complex solution (Imperial Jade Biotechnology Co., Ltd., Ningxia, China) with an enzyme concentration of 13.25 FPU g^{-1} biomass and xylanase of 8.4 U g^{-1} biomass, a solid loading of 3.3% (w/v). During the enzymatic hydrolysis, about 0.33 mL of 1% Tween-80 was simultaneously added, and the reaction was carried out with shaking at 50 °C and 150 rpm for 48 h. After the reaction was completed, the samples were centrifuged at 3000 g for 5 min, and the supernatant was collected for determination of soluble sugar content [37], all experiments were independently repeated three times. The calculation formula for enzymatic hydrolysis efficiency was described:

$$\textit{Enzymatic hydrolysis efficiency}\ (\%) = \frac{C}{N} \times 100\% \quad (1)$$

Where C represents the relative content of soluble sugars (% dry matter); N represents the cellulose content (% dry matter).

2.5. Determination of soluble sugars

For pentoses assay, the enzymatic hydrolysis supernatant was diluted with ultrapure water to a final volume of 1.0 mL in a 10 mL stoppered glass test tube. Reagent A (134.0 μL; 6.00 g orcinol dissolved in 100.0 mL of absolute ethanol) and Reagent B (2.0 mL; 0.100 g $FeCl_3$ dissolved in 100.0 mL of concentrated hydrochloric acid) were added sequentially. After vigorous mixing, the tube was heated in a boiling water bath for 20 min and subsequently cooled to room temperature. The absorbance was measured at 660 nm using a visible spectrophotometer, with

ultrapure water used as the blank.

For hexoses assay, the enzymatic supernatant was transferred into a 10 mL stoppered glass test tube and diluted with ultrapure water to a final volume of 1.0 mL. 2.0 mL of 0.20% (w/v) anthrone–sulfuric acid reagent was slowly added, followed by immediate vigorous mixing. The test tube was then heated in a boiling water bath for 5 min and cooled to room temperature under running tap water. The absorbance was measured at 620 nm using a visible spectrophotometer. A 1.0 mL aliquot of ultrapure water served as the blank.

2.6. Measurement of porosity by Congo red staining method

A dried sample (0.10 g) was mixed with phosphate buffer (pH 6.8) and varying volumes (0.25, 0.50, 0.75, 1.00, 1.50, and 2.00 mL) of Congo red solution (10 mg/mL), with the total volume adjusted to 10.0 mL. The mixtures were incubated at 60 °C for 24 h. After incubation, the samples were centrifuged for 5 min, and the absorbance of the supernatant was measured at 498 nm. The amount of Congo red adsorbed was determined from the difference between the initial dye concentration and the residual concentration in the supernatant.

2.7. Detection of degree of polymerization (DP) of cellulose

The degree of polymerization (DP) of cellulose was measured by capillary viscometry using an Ubbelohde viscometer (capillary diameter: 0.7–0.8 mm) [38]. The intrinsic viscosity ([η]) was derived from the relative viscosity (η_{rel}) based on the viscosity tables reported in the United States Pharmacopeia (USP 25/NF 20, 2002). The DP was then obtained using the modified Grobe equation:

$$DP = 190[\eta] \tag{2}$$

2.8. Ethanol fermentation

All yeast fermentations used *Saccharomyces cerevisiae*, which was purchased from Yichang Angel Yeast Co., Ltd. The yeast powder was dissolved in a phosphate buffer at pH 4.8 for 30 min to activate before use. Then, the yeast powder was suspended in a phosphate buffer at pH 4.8 to a final concentration of 0.5 g/L for all fermentation reactions, which were carried out at 37 °C for 48 h [39,40]. After the completion of ethanol fermentation, the mixture was centrifuged at 3000 g for 5 min [41]. The supernatant was collected, subjected to a 10-fold dilution, and then added to a biosensor analyzer (Xerman Technology) for ethanol determination. The calculation formula for ethanol yield is as follows:

$$\text{Ethanol yields } (\%) = \frac{A \times B}{1000} \times \frac{1}{M} \times 100\% \tag{3}$$

Where, *A* represents the total amount of ethanol (g/L); *B* represents the volume of the fermentation broth (mL); *M* represents the dry weight (g).

2.9. Lactic acid fermentation

Lactobacillus paracasei was used for all lactic acid fermentations. The strain was obtained from the Fermentation Engineering Laboratory, Huazhong Agricultural University, was used for lactic acid fermentation using sugars released from enzymatic hydrolysis. Anaerobic fermentation was conducted at 37 °C for 36 h with an initial inoculum adjusted to an OD_{600} of 0.5. After fermentation, the broth was centrifuged to collect the supernatant, which was diluted 10-fold prior to lactic acid quantification using a biosensor analyzer (Xerman Technology). The calculation formula for lactic acid yield is the same as that for the above-mentioned ethanol yield.

2.10. Assembly of biosorbents

2.10.1. Preparation of lignin nanoparticles (LNPs)

The supernatant obtained after pretreatment with 10% K_3PO_4 was collected and adjusted to pH 2 using 67% H_2SO_4 [42]. The mixture was left to stand overnight, and the resulting precipitate was dried in an oven at 60 °C. The dried solid was ground into powder, sieved through a 400-mesh screen, and collected as LNPs.

2.10.2. Preparation of oxidized cellulose nanofibers (CNFs)

Cellulose was extracted from the enzymatically hydrolyzed residue according to the method of [43]. About 3.0 g of crude fiber was placed into a ball-milling jar together with 20 small and 15 large steel balls, and the mixture was milled at 300 rpm for 4 h using a planetary ball mill. And the product was sieved through a 400-mesh screen to obtain cellulose nanofibers (CNF). Subsequently, 0.1 g of CNF was dispersed in 98 mL of distilled water under continuous stirring. A TEMPO-mediated oxidation was conducted by adding TEMPO (2,2,6,6-tetramethylpiperidin-1-oxyl, 0.016 g) and NaBr (0.1 g), while maintaining the pH at 10–11 using 1 M NaOH. The reaction proceeded at room temperature for 2 h and was quenched by adjusting the pH to 7 with 1 M HCl [44]. The product was thoroughly washed with distilled water until neutral, dried, and collected as oxidized CNFs.

2.10.3. Constructing hybrid of biosorbents

LNPs (0.1 g) and oxidized CNFs (0.1 g) were dispersed in 2 mL of 8% Tween-80 solution, followed by the addition of 10 mL of 0.45% H_2O_2. The mixture was shaken well and incubated at 50 °C with agitation at 150 rpm for 2 h. After the reaction, the suspension was centrifuged, and the supernatant was discarded. The precipitate was washed with distilled water to neutrality, dried at 60 °C, and ground into powder to obtain the biosorbent [45].

2.11. Adsorption experiments

Methylene blue (MB) and Congo red (CR) were prepared by dissolving the dyes in ultrapure water at room temperature (25 ± 1 °C), with initial concentrations of 25 mg/L and 50 mg/L, respectively. For adsorption experiments, 20 mL of dye solution was mixed with 20 mg of biosorbent or pretreated residue in a 50 mL centrifuge tube. The mixtures were shaken at 150 rpm for 4 h in a constant-temperature shaker. After adsorption, the suspensions were filtered, and the residual dye concentrations were determined using a UV–Vis spectrophotometer (V1100D, Shanghai MAPADA Instruments Co., Ltd.) at 664 nm for MB and 490 nm for CR. All experiments were performed in triplicate.

2.12. Isothermal adsorption models and kinetic models

The adsorption capacity (q_e, mg/g) of the dye is calculated by the following formula [46]:

$$q_e = \frac{(C_0 - C_e)^* V}{M} \tag{4}$$

Where, C_0 (mg/L) and C_e (mg/L) indicate the concentration of MB or CR at initial and equilibrium. The volume of the solution is expressed as *V* (L) and the mass of the sample is expressed as *M* (mg).

The correlation between adsorption capacity (q_e, mg/g) and the concentration of MB, CR (C_e, mg/L) at equilibrium was modeled using three isotherms. The Langmuir isothermal equation is given below [47]:

$$q_e = \frac{q_{max} K_L C_e}{1 + K_L C_e} \tag{5}$$

Among them, q_{max} refers to the maximum adsorption capacity (mg/g), K_L represents the Langmuir isothermal constant, and indicates the adsorption capacity of biosorbent for MB.

The Freundlich isotherm equation is stated as follow:

$$q_e = K_F C_e^{1/n} \tag{6}$$

Where, K_F is the Freundlich isotherm constant, and $1/n$ is the heterogeneity factor.

Representing equation of Temkin model is as follow:

$$q_e = \frac{RTln(A_T C_e)}{b_T} \tag{7}$$

Where, A_T refers to the equilibrium constant, b_T is the Temkin constant related to adsorption heat, R is the universal gas constant, and T is the absolute temperature (K).

The kinetic models were applied to predict the relationship between adsorption capacity at equilibrium (q_e, mg/g) and adsorption for t hours (q_t, mg/g). The pseudo 1st order model (8) and pseudo 2nd order model (9) are represented as follows:

$$ln(q_e - q_t) = ln\, q_t - K_1 t \tag{8}$$

$$\frac{t}{q_t} = \frac{1}{K_2 q_e^2} + \frac{t}{q_e} \tag{9}$$

Where, K_1 and K_2 are the pseudo 1st order and pseudo 2nd order constants, respectively.

The Weber–Morris intraparticle diffusion model is stated as:

$$q_t = K_{ip} t^{0.5} + C \tag{10}$$

Where, K_{ip} is intraparticle diffusion apparent adsorption rate constant, C is a constant related to the boundary layer thickness.

2.13. Adsorption thermodynamic model

The thermodynamic parameters Gibbs free energy (ΔG, kJ/mol), adsorption enthalpy (ΔH, kJ/mol), and adsorption entropy (entropy (ΔS, kJ/mol) during the MB adsorption process can be calculated via Eqs. (11) and (12).

$$\Delta G = -\mathrm{R}TlnKL \tag{11}$$

$$ln\, K_L = \frac{\Delta S}{R} - \frac{\Delta H}{\mathrm{R}T} \tag{12}$$

2.14. Characterization

Cellulose crystalline index (CrI) was characterized by X-ray diffraction (XRD) method. Powdered samples were evenly spread on a glass slide and analyzed using an X-ray diffractometer equipped with Cu Kα radiation (λ = 1.54056 Å), operated at 40 kV and 30 mA. Diffraction patterns were recorded over a 2θ range of 10–40°, with a scanning rate of 5° min^{-1} and a step size of 0.02°. The crystallinity index was calculated using the Segal method according to the following equation:

$$CrI(\%) = \frac{I_{200} - I_{am}}{I_{200}} \times 100\% \tag{13}$$

Where, I_{200} is the maximum intensity of the (200) crystalline peak, and I_{am} is the intensity of the amorphous background measured at around 2θ ≈ 18°.

The surface morphology and cross-sectional structure of the synthesized biosorbents were examined using scanning electron microscopy (SEM). The samples were dried at 60 °C prior to analysis, fractured to expose fresh cross-sections, and mounted on conductive adhesive tape with the cross-section facing upward. The samples were sputter-coated with a thin layer of gold under vacuum before observation. SEM images were acquired under high-vacuum conditions at appropriate accelerating voltages using a slow-scan imaging mode.

Fourier transform infrared (FTIR) spectroscopy was employed to identify the functional groups of the samples. Approximately 0.1 g of sample powder was prepared as a pellet and analyzed over the wavenumber range of 4000–400 cm^{-1}, with 32 scans collected per sample. Air was used as the background and subtracted automatically during measurement. Functional groups were qualitatively identified based on characteristic absorption bands.

Fluorescence microscopy was used to observe the cellulose structure of the biosorbents. A small amount of sample was dispersed in sterile normal saline to form a homogeneous suspension, followed by staining with Calcofluor White solution. The mixture was incubated in the dark at room temperature for 10 min. An aliquot (10 μL) of the stained suspension was placed on a glass slide, covered with a coverslip, and observed under a fluorescence microscope using a UV excitation channel. Fluorescence images were captured after appropriate focusing [48].

2.15. Statistical analysis

Analysis of variance (ANOVA), regression coefficients, and Spearman rank correlation coefficients were performed using SPSS 16.0 (Inc., Chicago, IL). Line charts, bar charts, and regression analyses of the best-fit curves were plotted using Origin 8.5 software (Microcal Software, Northampton, MA).

3. Results and discussion

3.1. Optimization of green alkaline salt pretreatment for efficient saccharification

To establish an efficient saccharification platform for *Miscanthus* biomass, the initial cell wall composition of four *Miscanthus* varieties (Mlu10, Msa21, Msa22, and Msa32) was screened and characterized. The analysis revealed significant compositional differences among the varieties (Fig. S1), with cellulose contents ranging from 33.26% to 43.25%, and the most pronounced disparity observed between Mlu10 and Msa22. The lignin contents of the four accessions were varied from 21.30% to 23.37%. As lignin is a major barrier in biorefinery processes, its variations should mainly affect pretreatment performance and subsequent enzymatic hydrolysis efficiency. Despite cellulose content determines glucose production, the content and structural complexity of lignin act as the primary recalcitrant factors by physically blocking enzyme accession and non-productively adsorbing cellulases. Therefore, a favorable balance between high cellulose availability and low lignin recalcitrance is essential, underscoring the necessity of adopting tailored pretreatment strategies to maximize carbohydrate release.

Based on these results, Mlu10 and Msa21 were selected as representative substrates for a systematic investigation of the effects of salt concentration and reaction time on enzymatic hydrolysis, using potassium phosphate (K_3PO_4) and potassium carbonate (K_2CO_3) as green alkaline pretreatment agents. Experimental findings demonstrated a typical unimodal trend for both variables: enzymatic efficiency peaked at a salt concentration of 10% (Fig. 1B & D) and a reaction time of 2.5 h (Fig. 1C & E). Moderate pretreatment intensity effectively removed lignin and enhanced cellulose accessibility, whereas excessive severity led to the formation of fermentation inhibitors such as furfural, thereby diminishing enzymatic activity. In terms of salt species, K_3PO_4 outperformed K_2CO_3 significantly, achieving a maximum saccharification efficiency of 81.22% (14.39 g/L), which was 32.5% higher than that of K_2CO_3. This enhancement is primarily attributed to the stronger hydrolytic capacity of PO_4^{3-} ions released by K_3PO_4, which generate a higher concentration of OH^-, facilitating more thorough lignin removal [49]. Substrate performance evaluation further revealed that Msa21 consistently exhibited superior enzymatic digestibility and total sugar yield compared to Mlu10 across all pretreatment conditions (Table S1–S2). Under optimal conditions, Msa21 achieved a total sugar yield of 47.31%, which was 35.6% higher than that of Mlu10 (Fig. 1F).

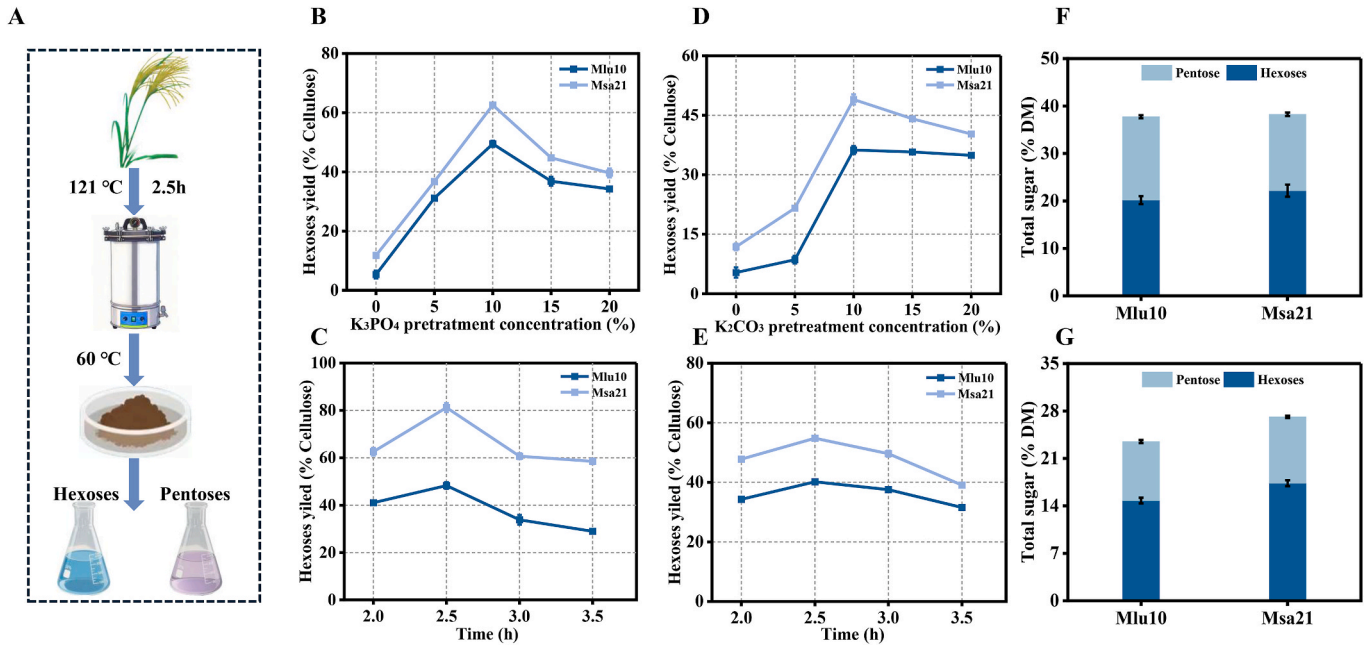

Fig. 1. Optimization of *Miscanthus* pretreatment with green alkaline salts. (A) Schematic diagram of the pretreatment process; (B, D) Sugar yields obtained after pretreatment with different concentrations of K_3PO_4 and K_2CO_3; (C, E) Sugar yields at various pretreatment times with 10% K_3PO_4 and K_2CO_3; (F) Total sugar yield at the optimal pretreatment concentration; (G) Total sugar yield at the optimal pretreatment time (n = 3). DM: dry matter. (For interpretation of the references to color in this figure legend, the reader is referred to the Web version of this article.)

This performance gap highlighted the strong correlation between feedstock composition and saccharification potential; the superior sugar release in Msa21 is likely driven by its higher initial cellulose loading and a more porous cell wall structure following delignification, which should mitigate the physical barriers limiting enzymatic attack. In contrast, the lower cellulose content and potentially more recalcitrant lignin-carbohydrate complexes in Mlu10 restricted its hydrolysis efficiency, confirming its greater potential as a feedstock for saccharification-based bioprocessing.

Overall, pretreatment with 10% K_3PO_4 for 2.5 h proved optimal for

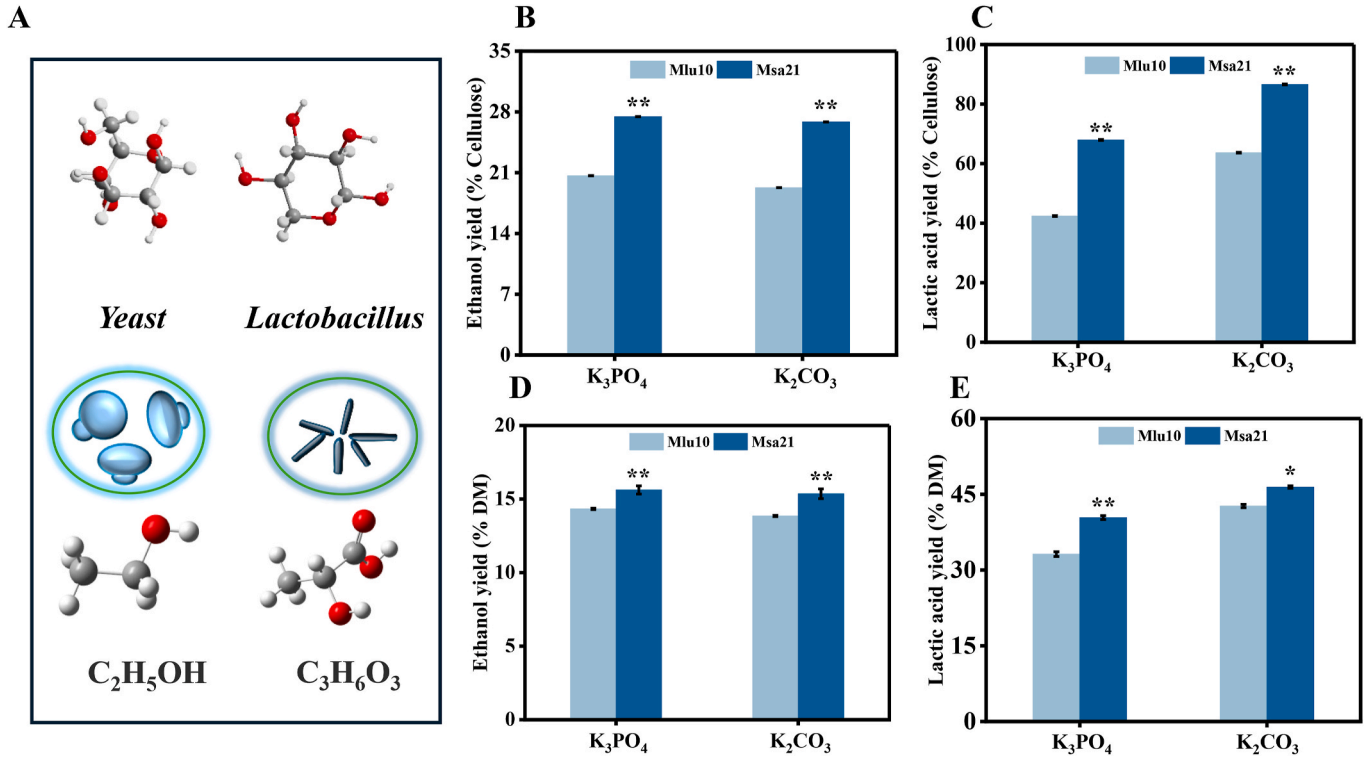

Fig. 2. Fermentation of hydrolysates for sugar and lactic acid production.(A) Schematic diagram of the fermentation process; (B, C) Ethanol and lactic acid yields (% cellulose) under the optimal pretreatment conditions (10% K_3PO_4 or K_2CO_3, 2.5 h); (D) Theoretical ethanol yield; (E) Theoretical lactic acid yield. * and ** indicate significant differences between two *Miscanthus* varieties at $p < 0.05$ and 0.01, respectively (n = 3).

maximizing saccharification efficiency, establishing a robust platform for subsequent fermentation studies.

3.2. Regulation of ethanol and lactic acid yields by green pretreatment

Building upon the optimized saccharification platform, the potential of *Miscanthus* biomass for fermentative production of biofuels (ethanol) and platform chemicals (lactic acid) was further evaluated, with a focus on elucidating the regulatory effects of pretreatment agents on the fermentation pathways (Fig. 2). The K_3PO_4-pretreated hydrolysates exhibited significantly higher ethanol yields (20.65%–27.46%) (7.215 g/L–7.81 g/L) compared to those pretreated with K_2CO_3 (Fig. 2B), primarily attributed to their higher fermentable sugar content and enhanced pH buffering capacity during fermentation. This improvement can be ascribed to the more effective lignin removal and increased sugar availability conferred by K_3PO_4, which collectively created a more favorable metabolic environment for ethanol fermentation.

Conversely, lactic acid fermentation exhibited an opposite trend. The K_2CO_3-pretreated group achieved lactic acid yields of 42.39%–67.95% (% cellulose), substantially surpassing the K_3PO_4-treated samples. This observation suggests that although K_3PO_4 facilitates greater sugar release, the presence of PO_4^{3-} ions exerts an inhibitory effect on the metabolic activity of lactic acid bacteria, thereby altering the product distribution towards ethanol at the expense of lactic acid synthesis [50].

Notably, regardless of the target fermentation product, Msa21 consistently outperformed Mlu10 in terms of product yields. Specifically, Msa21 exhibited an increase of 9.0%–10.9% in ethanol yield and 8.8%–21.8% in lactic acid yield compared to Mlu10 (Fig. 2D & E), further corroborating its superiority as a feedstock for biomass fermentation. Additionally, co-pretreatment experiments combining 10% K_3PO_4 and 10% K_2CO_3 (Fig. S2) demonstrated similar trends to those observed in the single-agent treatments, thereby reinforcing the pivotal role of pretreatment agent selection in steering the distribution of fermentation products.

These findings demonstrate that green pretreatment agents not only enhance the fermentation efficiency of *Miscanthus* biomass but also enable precise regulation of product distribution, offering a viable strategy for directing biomass conversion towards specific high-value products.

3.3. Enhanced lignin removal and structural modification via green alkaline salt pretreatment

To evaluate the impact of alkaline salts on the structural integrity of *Miscanthus* lignocellulose, scanning electron microscopy (SEM) was employed to observe the microstructural morphology of raw and pretreated samples (Fig. 3A). The untreated *Miscanthus* stalks exhibited a dense, smooth surface lacking visible porosity. In contrast, after alkaline salt pretreatment, the lignocellulosic matrix was visibly disrupted, characterized by surface roughness and exfoliation. Particularly under K_3PO_4 treatment, the stalks underwent extensive structural degradation, generating numerous fine particulate and lamellar fragments, indicative of K_3PO_4 superior delignification capability as a stronger alkaline salt.

To elucidate the chemical composition changes induced by pretreatment, cell wall compositional analysis (Fig. 3B & C) revealed that lignin content decreased by 44.8%–67.2% after pretreatment, with K_3PO_4 achieving the highest removal (64%–67%). Monomeric lignin analysis (Fig. 3D & E, Table S3) indicated a reduction in H-monomer after K_3PO_4 pretreatment, thereby elevating the S/G ratio in the residual biomass and loosening the lignocellulosic structure, which in turn is favorable for enzymatic hydrolysis. Total phenolic content of lignin from pretreatment supernatant (Fig. 3F) revealed that Msa21 consistently

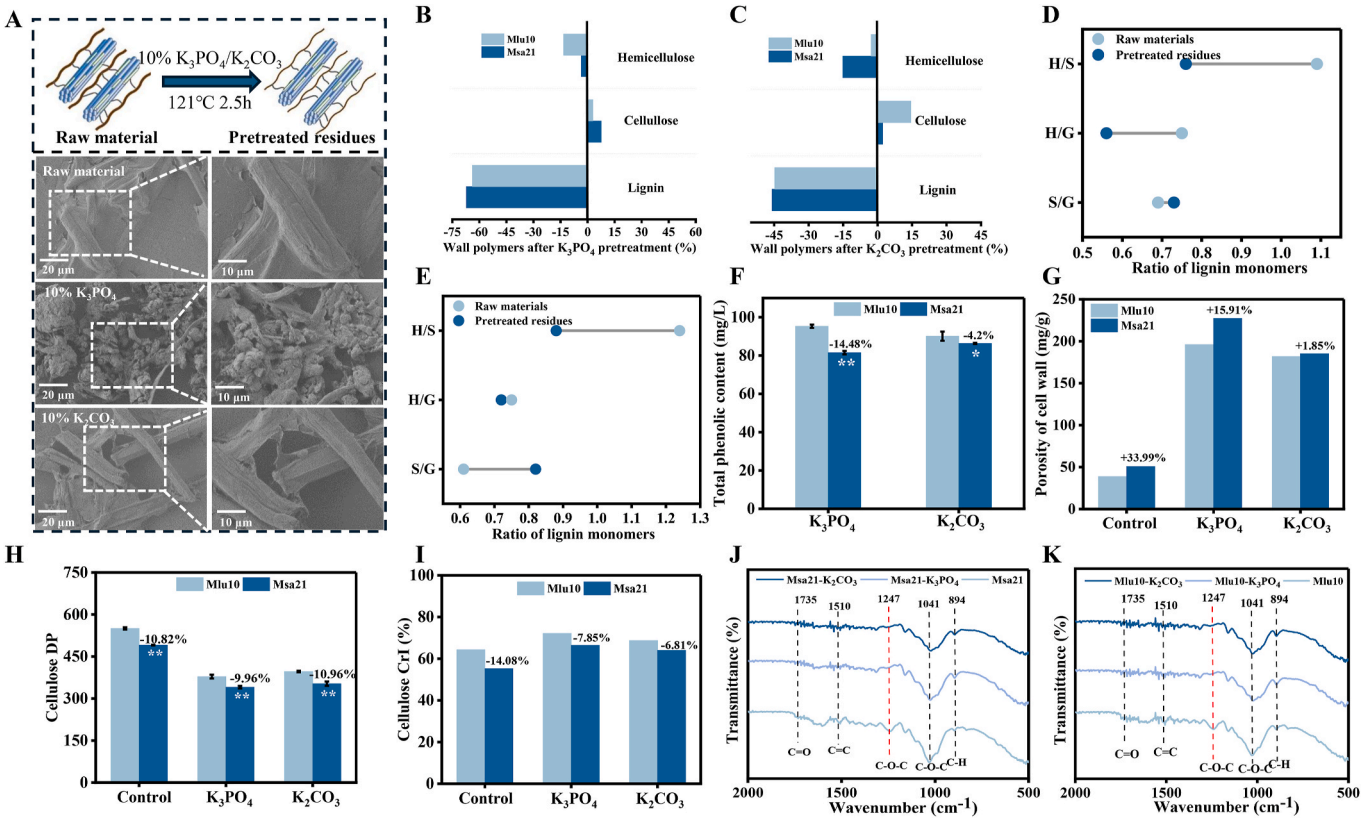

Fig. 3. Characteristics of *Miscanthus* straws before and after pretreatment. (A) SEM images of Msa21 before and after K_3PO_4/K_2CO_3 pretreatment; (B, C) Cell wall composition of pretreated samples compared with the raw materials; Mlu10 (D) and Msa21 (E) lignin monomer after pretreatment compared with the raw materials; (F) Total phenolic content of lignin from pretreatment supernatant; (G) Cell wall porosity; (H) Degree of polymerization (DP) of cellulose; (I) Crystallinity index (CrI) of cellulose; FTIR spectra of Mlu10 (J) and Msa21 (K). * and ** indicate significant differences between two samples at $p < 0.05$ and 0.01, respectively (n = 3).

exhibited 4.2%–14.48% lower total phenol levels than Mlu10. This finding suggests that alkaline salt pretreatment of Mlu10 facilitated the release of more H monomers (Table S3), indicating a higher adsorption activity. As the relatively higher proportion of H monomers in lignin is accountable for the lower degree of cross-linking of its molecular chains, it is easier to form a porous structure during the preparation of lignin nanoparticles (LNPs) or adsorbents, which could provide more physical adsorption sites for adsorbates and shortens their intraparticle diffusion paths.

Porosity measurements (Fig. 3G & Fig. S3) further confirmed that pretreatment enhanced material porosity by 2.6–4.5-fold, with the K_3PO_4-treated samples exhibiting the highest values (196.07–227.27 mg/g). These results corroborated the SEM observations, demonstrating that K_3PO_4 more effectively disrupted the stalk structure and promoted lignin removal. Across different *Miscanthus* cultivars, Msa21 exhibited 2.6%–5.2% higher lignin removal and 1.85%–33.99% greater porosity increased than Msa10, suggesting greater cell wall sensitivity to alkaline salts and making it a promising bioenergy feedstock. Further analysis revealed that the degree of polymerization (DP) decreased by 28.4% in Mlu10 and 47.1% in Msa21 after pretreatment (Fig. 3H), with Msa21 consistently maintaining lower DP values, thereby facilitating cellulose depolymerization and sugar release (Fig. 1). As cellulose crystallinity (CrI) was decreased after pretreatment (Fig. 3I & Fig. S4), it was likely due to partial disruption of the crystalline cellulose structure, although some amorphous component such as lignin was removed. FTIR analysis (Fig. 3J & K) further confirmed lignin removal, as both K_3PO_4 and K_2CO_3 markedly attenuated characteristic lignin peaks (C=O at 1735 cm^{-1}, C=C at 1627/1510 cm^{-1}, C–O–C and C–H at 894 cm^{-1}, and 1247 cm^{-1}), with the 1247 cm^{-1} peak disappearing completely after pretreatment.

Altogether, K_3PO_4 pretreatment substantially disrupts the *Miscanthus* cell wall, efficiently removes lignin, enhances porosity, and reduces polymerization degree, thereby laying a solid foundation for subsequent high-efficiency enzymatic hydrolysis. Particularly for Msa21, its high cell wall sensitivity confers superior bioconversion potential after pretreatment.

3.4. Mechanistic insights into CNF-LNP composite assembly

Efficient lignin removal not only enhanced cellulose enzymatic hydrolysis but also yielded large quantities of recoverable lignin nanoparticles (LNPs), providing a key feedstock for biosorbent fabrication. In this study, LNPs recovered from the pretreatment supernatant and cellulose nanofibers (CNFs) isolated from the solid residue were co-assembled into CNFs–LNPs composite adsorbents (Fig. 4). The effect of CNFs/LNPs ratios on adsorption performance was first examined. Increasing the CNF proportion initially improved adsorption capacity but subsequently caused a decline once the ratio exceeded 2:2, as excessive CNF encapsulation shielded LNP active sites and densified the composite structure (Fig. S5). Crosslinker optimization showed that 0.45% H_2O_2 achieved the highest capacity. Moderate H_2O_2 induced mild LNP surface oxidation, introducing hydrophilic groups that enhanced CNFs–LNPs interfacial bonding, whereas excessive oxidation degraded LNPs and reduced performance (Fig. S6). To improve structural stability, Tween-80 was introduced as a coupling agent. Its hydrophilic moieties formed hydrogen bonds with CNF hydroxyls, while hydrophobic tails engaged in π–π interactions with LNPs aromatic rings, enhancing dispersion and suppressing aggregation. Adsorption capacity increased with Tween-80 concentration from 2% to 8% (v/v), beyond

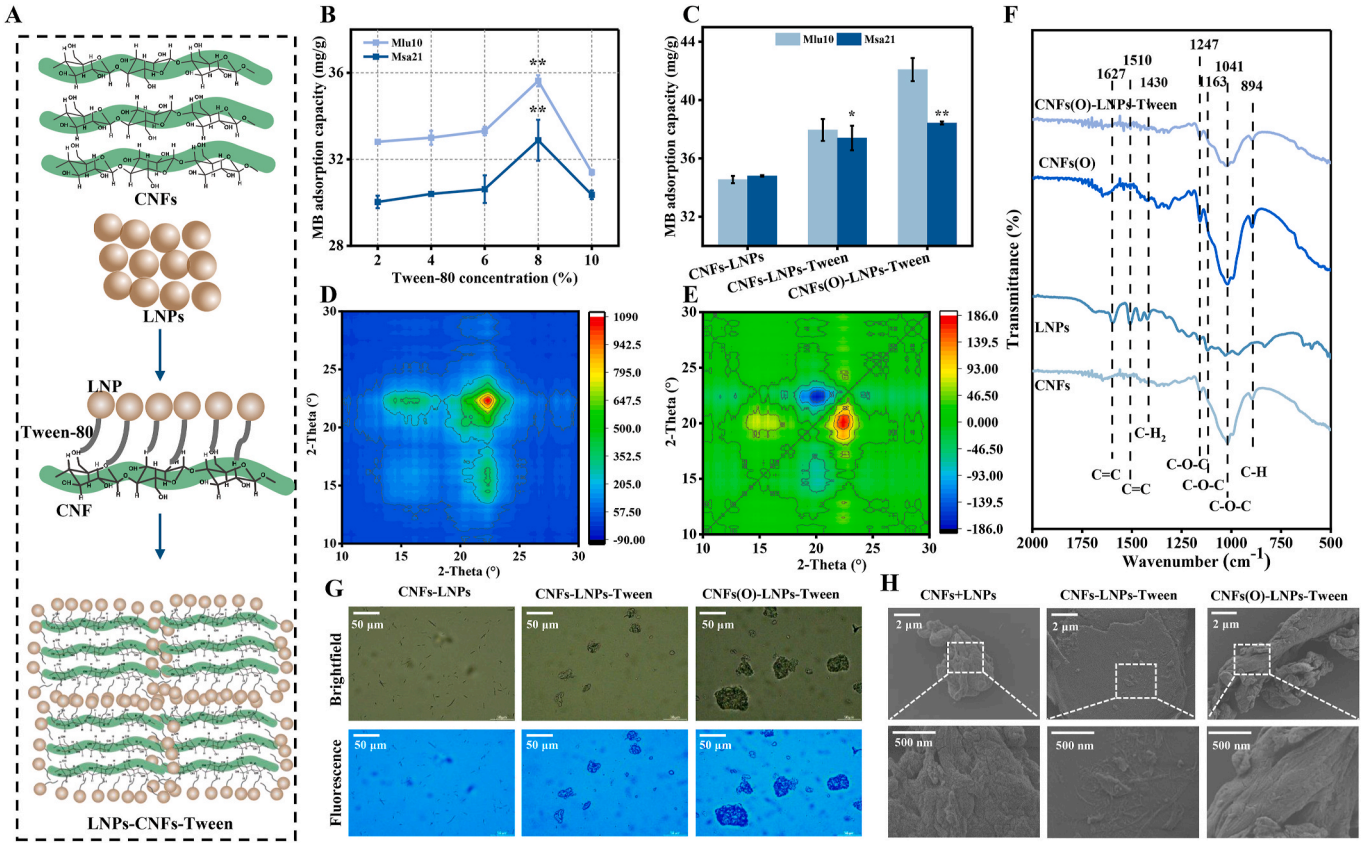

Fig. 4. Assembly of CNFs–LNPs biosorbents. (A) Schematic diagram of adsorbent assembly; (B) Effect of different Tween-80 concentrations on MB adsorption by the biosorbents; (C) MB adsorption of three biosorbents; (D)(E) Synchronous and asynchronous XRD spectra of Mlu10 biosorbent as prepared at Fig. S7; (F) FTIR spectra of LNPs, CNFs, CNFs(O), CNFs–LNPs, and CNFs(O)–LNPs; (G) Fluorescence microscopy image of the adsorbent; (H) SEM image of the biosorbents. * and ** indicate significant differences between two samples at $p < 0.05$ and 0.01, respectively (n = 3). Adsorption conditions: C_{MB} = 50 mg/L, time = 4 h. CNFs(O) represents CNFs oxidized by TEMPO.

which over-encapsulation slightly reduced performance, making 8% optimal (Fig. 4B). Additional TEMPO-mediated oxidation of CNFs further enhanced adsorption, particularly in Mlu10-based composites (Fig. 4C).

X-ray diffraction (XRD) analysis (Fig. S7) showed that Tween-80 markedly increased composite crystallinity. Two-dimensional correlation spectroscopy (2D-COS XRD) (Fig. 4D & E Fig. S7) revealed synchronous positive correlations between 18° and 22.5° peaks, indicating cooperative reorganization of crystalline and amorphous domains under Tween-80 modulation. Asynchronous spectra confirmed that crystalline regions responded first to external perturbations, subsequently driving amorphous reordering. FTIR spectra (Fig. 4F) confirmed the formation of chemical bonds (C-O-C) between CNFs and LNPs, reinforcing the structural and functional stability of the composites. Fluorescence microscopy revealed distinct morphological transformations among the three types of biosorbents (Fig. 4G). With the incorporation of Tween-80, CNFs and LNPs assembled into larger adsorptive particles, whose size further increased upon CNFs oxidation, thereby enhancing the adsorption performance. Under UV excitation, pronounced lignin-associated fluorescence was observed on the composite surface, confirming the encapsulation of CNFs by LNPs. SEM images (Fig. 4H) illustrated that composites without surfactant formed dense, irregular aggregates with low porosity. Incorporating 8% Tween-80 produced uniform, film-like morphologies with reduced aggregation, though partial collapse occurred during drying. In contrast, TEMPO-oxidized CNFs(O) composites formed highly porous, three-dimensional nanofiber networks via electrostatic repulsion-driven self-assembly, ensuring high surface area, structural integrity, and uniform LNPs immobilization.

3.5. Adsorption performance and mechanism of CNFs-LNPs biosorbents

The adsorption performance and underlying mechanism of CNF–LNP biosorbents were evaluated using methylene blue (MB) as a model pollutant (Fig. 5). UV–Vis spectra (Fig. 5A) revealed a pronounced decrease in MB absorbance after adsorption, with Mlu10 consistently showing lower residual intensities than Msa21, indicating superior dye removal efficiency. As the initial MB concentration increased from 20 to 200 mg/L, the adsorption capacity rose from 22.15 to 59.65 mg/g. Across all concentrations, Mlu10 maintained a higher adsorption capacity than Msa21. Isotherm fitting (Fig. 5B–E, Table 1) showed that, although the Freundlich model (R^2>0.980) described the data well, the Langmuir model achieved the best fit (R^2>0.989), indicating predominantly monolayer chemisorption, with minor contributions from van der Waals-driven physisorption. Temkin model results (R^2 = 0.9659–0.9731) further supported chemisorption dominance. The maximum Langmuir capacities for Mlu10 and Msa21 were 59.5 and 43.4 mg/g, respectively—a 37.1% improvement for Mlu10.

Temperature-dependent experiments (Fig. 5F) showed decreasing adsorption with increasing temperature, confirming an exothermic process. Van't Hoff analysis (Fig. 5G–Table 2) yielded negative Gibbs free energy changes (ΔG) for both materials, with more negative values for Mlu10, indicating stronger spontaneity and affinity. Negative enthalpy (ΔH) and entropy (ΔS) changes indicated exothermic adsorption accompanied by reduced system randomness. These thermodynamic trends, together with FTIR observations of functional group interactions and SEM images showing 3D CNFs-LNPs network, were consistent with directional intermolecular interactions such as hydrogen bonding and π–π stacking between surface functional groups and dye molecules, although these interactions were inferred indirectly from the data. The lower absolute ΔH and ΔS values for Mlu10 further suggested a higher density of accessible active sites, corresponding to its greater adsorption efficiency.

Kinetic studies showed rapid uptake within 50 min, reaching equilibrium at ~90 min (Fig. 5H). Pseudo-second-order kinetics provided the best fit (Fig. S9, Table S4–S5), confirming chemisorption control. Additional tests with Cr (VI) ions (Fig. S10) demonstrated a 1.58-fold higher adsorption capacity for Mlu10 over Msa21, underscoring its potential for both dye removal and heavy metal remediation.

Collectively, Mlu10-derived CNFs–LNPs biosorbents, characterized by abundant active sites and optimized microstructure, exhibited high-efficiency dye and heavy metal removal via coordination-driven chemisorption, highlighting their promise as sustainable functional adsorbents for environmental applications.

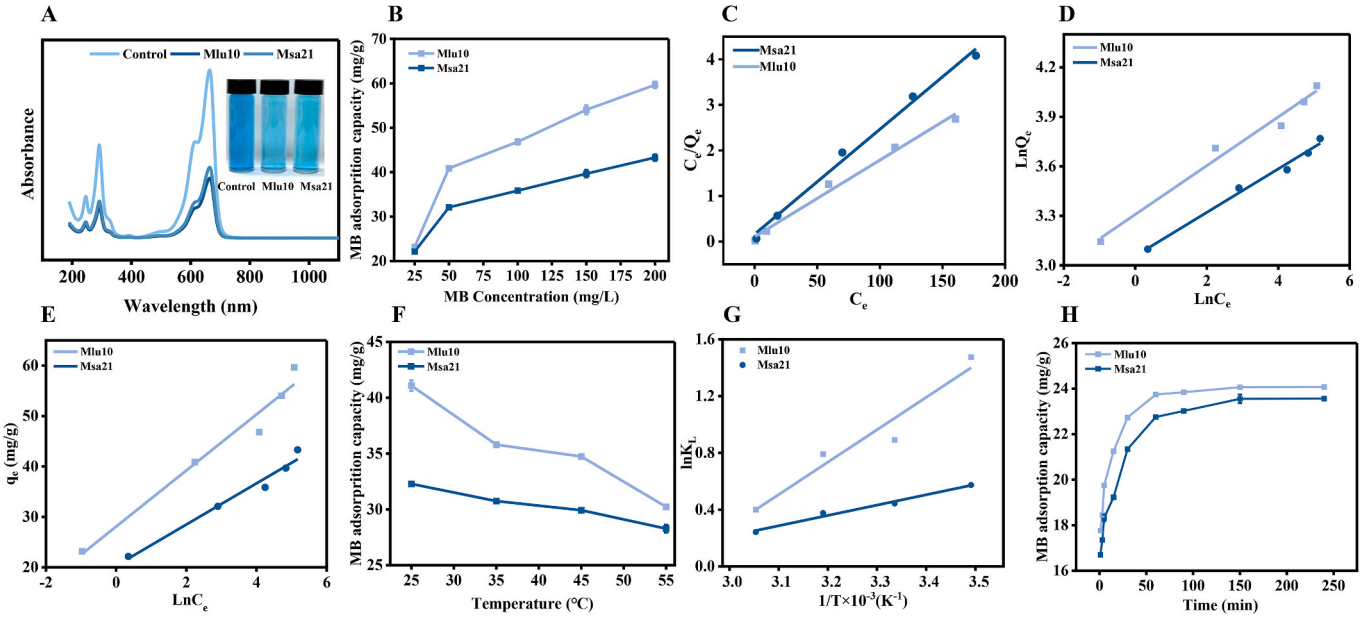

Fig. 5. Performance of the biosorbents.(A) UV–Vis full spectra of methylene blue (MB) adsorption by the adsorbents; (B) Adsorption capacities of the adsorbents at different MB concentrations; (C–E) Isothermal adsorption model fitting using Langmuir (C), Freundlich (D), and Temkin (E) models; (F) MB adsorption capacities of the adsorbents at different temperatures; (G) Thermodynamic parameters of the adsorbents; (H) MB adsorption capacities of the adsorbents at different times. (For interpretation of the references to color in this figure legend, the reader is referred to the Web version of this article.)

Table 1
Parameters of isothermal adsorption model fitting.

Samples	Langmuir			Freundlich			Temkin		
	q_{max} (mg/g)	b (L/mg)	R^2	K_F	$1/n$	R^2	b_t(mg/g)	k_t(L/mg)	R^2
Mlu10	59.524	0.1055	0.9893	27.344	0.1478	0.9803	5.5621	28.07	0.9659
Msa21	43.422	0.1613	0.9926	21.264	0.1318	0.9875	4.0806	20.31	0.9731

Table 2
Thermodynamic parameters of adsorption.

Samples	T	K	R^2	$\Delta G°$ (kJ mol^{-1})	$\Delta H°$ (kJ mol^{-1})	$\Delta S°$ (kJ mol^{-1})
Mlu10	298.15	4.37	0.9399	−3.655	−27.11	−79.28
Msa21	298.15	1.77	0.9844	−1.422	−8.641	−24.23

3.6. Component distribution and product yields of Miscanthus varieties

The component distribution and product yields from two *Miscanthus* varieties, Mlu10 and Msa21, were evaluated on a basis of 1000 g of initial dry biomass (Fig. 6). Mlu10 possessed a higher cellulose content (432.5 g) than Msa21 (332.6 g), whereas their lignin contents were comparable. Following pretreatment, a majority of the lignin was solubilized into the supernatant (175.2 g for Mlu10; 163.3 g for Msa21), while cellulose and hemicellulose were predominantly retained in the solid residue. Subsequent enzymatic hydrolysis of this residue released significantly higher amounts of pentoses and hexoses from Msa21 (185.4 g and 287.2 g, respectively) compared to Mlu10 (154.4 g and 197.0 g, respectively). While both varieties generated similar quantities of lignin nanoparticles (LNPs) and cellulose nanofibrils (CNFs), their performance diverged in downstream applications. Mlu10 yielded more biosorbent (109.4 g), whereas Msa21 exhibited superior fermentation efficiency, resulting in a higher lactic acid yield (226 g). Ethanol production was comparable between the two varieties. Overall, the results reveal a critical trade-off: the higher initial cellulose content of Mlu10 favored biosorbent production, while the superior sugar-release efficiency of Msa21 made it the preferred candidate for lactic acid fermentation.

4. Conclusion

This study aims to explore a green and integrated biorefinery of *Miscanthus* biomass for high productivity of fermentable sugars, biofuels, organic acids, and functional materials. In general, green alkaline salt pretreatment (10%, 121 °C, 0.1 MPa, 2.5 h) enables maximum lignin removal (67.2%) for significantly increasing lignocellulose porosity and reducing cellulose polymerization, leading to a remarkably enhanced biomass enzymatic saccharification in two *Miscanthus* accessions (Msa21, Mlu10). In comparison, the Msa21 accession shows superior sugar release for lactic acid and ethanol fermentations at high yields, whereas the Mlu10 rich at cellulose content is effective for generation of CNFs–LNPs biosorbents. In particular, the distinct CNFs–LNPs composites constructed by TEMPO-mediated CNF oxidation combined with Tween-80-assisted coupling, are of characteristically adsorbing

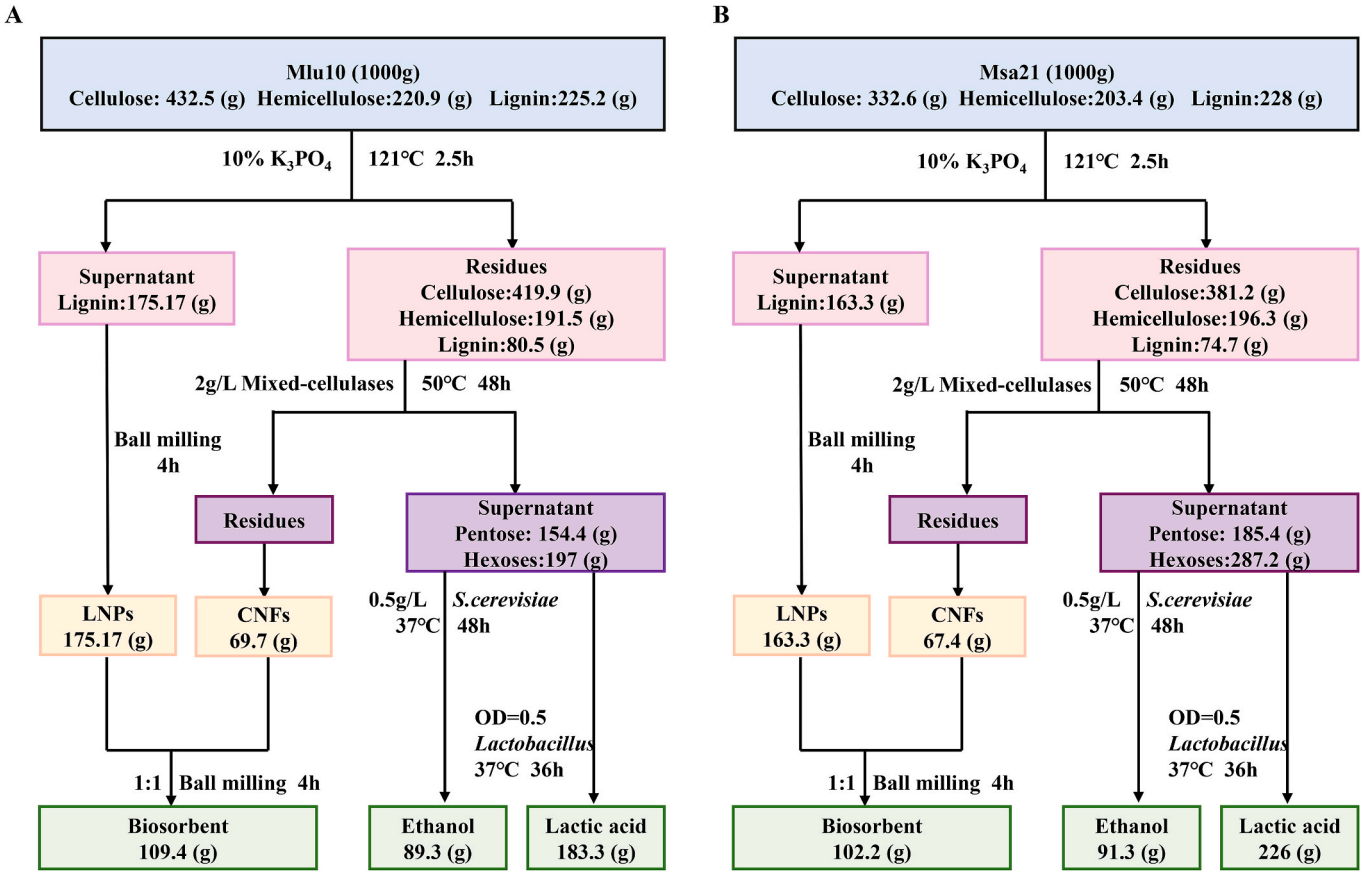

Fig. 6. Comparative component distribution and product yields of Mlu10 and Msa21 after fractionation and conversion.

capacities for removals of industry dyes and heavy metal ions via a primary chemisorption mechanism. Therefore, this work has demonstrated a powerful strategy for enhancing biomass enzymatic saccharification towards bioethanol and biochemicals conversions at high yields along with bioproducts generation at high performance, providing an applicable technology for both biorefinery and environmental remediation using *Miscanthus* and other bioenergy crops.

CRediT authorship contribution statement

Bing Gao: Methodology, Investigation, Visualization, Software, Writing – original draft. **Junsheng Yu:** Methodology, Investigation, Software, Writing – original draft. **Ling Luo:** Methodology, Investigation, Software, Writing – original draft. **Lei Zhu:** Methodology, Investigation, Software, Writing – original draft. **Zongtai Tang:** Methodology, Investigation, Software, Writing – original draft. **Yongtai Wang:** Investigation, Writing – review & editing. **Jiacheng Kang:** Investigation, Writing – review & editing. **Dan Sun:** Software, Methodology, Investigation. **Hao Peng:** Software, Methodology, Investigation. **Yanting Wang:** Writing – review & editing, Funding acquisition. **Liangcai Peng:** Conceptualization, Supervision, Writing – review & editing, Funding acquisition. **Hua Yu:** Supervision, Methodology, Writing – review & editing, Funding acquisition.

Declaration of competing interest

The authors declare that they have no known competing financial interests or personal relationships that could have appeared to influence the work reported in this paper.

Acknowledgements

This work was supported by the National Natural Science Foundation of China (32500325, 32470273), Hubei Provincial Natural Science Foundation of China for Excellent Young Scientists (2024AFA100), the Doctoral Research Start-up Fund of Hubei University of Technology (XJ2024000402), the Initiative Grant of Hubei University of Technology for High-level Talents (GCC20230001).

Appendix A. Supplementary data

Supplementary data to this article can be found online at https://doi.org/10.1016/j.renene.2026.125555.

References

[1] W.B. Yang, B.Y. He, H. Yu, H.Y. Zhang, Y.N. Li, J.Y. Liu, H. Peng, H.L. Wang, P. Liu, Y.T. Wang, L.C. Peng, D. Sun, An optimal conversion cascading of distinct lignocelluloses to maximize bioethanol productivity and bio-adsorption capacities of Cd^{2+}/Cr(VI) and red/blue dyes selective for complete biomass recycling, Int. J. Biol. Macromol. 321 (2025) 146214, https://doi.org/10.1016/j.ijbiomac.2025.146214.

[2] Y.M. Wang, P. Liu, G.F. Zhang, Q.M. Yang, J. Lu, T. Xia, L.C. Peng, Y.T. Wang, Cascading of engineered bioenergy plants and fungi sustainable for low-cost bioethanol and high-value biomaterials under green-like biomass processing, Renew. Sustain. Energy Rev. 137 (2021) 110586, https://doi.org/10.1016/j.rser.2020.110586.

[3] D. Sun, Q.M. Yang, Y.T. Wang, H.R. Gao, M.X. He, X.C. Lin, J. Lu, Y.M. Wang, H. Kang, A. Alam, Y.Y. Tu, T. Xia, L.C. Peng, Distinct mechanisms of enzymatic saccharification and bioethanol conversion enhancement by three surfactants under steam explosion and mild chemical pretreatments in bioenergy *Miscanthus*, Ind. Crop. Prod. 153 (2020) 112559, https://doi.org/10.1016/j.indcrop.2020.112559.

[4] H. Peng, W.Y. Zhao, J.Y. Liu, P. Liu, H.Z. Yu, J. Deng, Q.M. Yang, R. Zhang, Z. Hu, S.L. Liu, D. Sun, L.C. Peng, Y.T. Wang, Distinct cellulose nanofibrils generated for improved pickering emulsions and lignocellulose-degradation enzyme secretion coupled with high bioethanol production in natural rice mutants, Green Chem. 24 (2022) 2975–2987, https://doi.org/10.1039/D1GC04447H.

[5] P. Liu, A. Li, Y.M. Wang, Q.M. Cai, H.Z. Yu, Y.Q. Li, H. Peng, Q. Li, Y.T. Wang, X. Y. Wei, R. Zhang, Y.Y. Tu, T. Xia, L.C. Peng, Distinct *Miscanthus* lignocellulose improves fungus secreting cellulases and xylanases for consistently enhanced biomass saccharification of diverse bioenergy crops, Renew. Energy 174 (2021) 799–809, https://doi.org/10.1016/j.renene.2021.04.107.

[6] F. Liu, J.Y. Li, H. Yu, Y.Q. Li, Y.T. Wang, H.R. Gao, H. Peng, Z. Hu, H.L. Wang, G. F. Zhang, Y.Y. Tu, L.C. Peng, Optimizing two green-like biomass pretreatments for maximum bioethanol production using banana pseudostem by effectively enhancing cellulose depolymerization and accessibility, Sustain. Energy Fuels 5 (2021) 3467–3478, https://doi.org/10.1039/D1SE00613D.

[7] M. Sriariyanun, M.P. Gundupalli, V. Phakeenuya, T. Phusamtisampan, Y.S. Cheng, P. Venkatachalam, Biorefinery approaches for production of cellulosic ethanol fuel using recombinant engineered microorganisms, J. Appl. Sci. Eng. 27 (2023) 1985–2005, https://doi.org/10.6180/jase.202402_27(2).0001.

[8] S. Areeya, E.J. Panakkal, P. Kunmanee, A. Tawai, S. Amornraksa, M. Sriariyanun, A. Kaoloun, N. Hartini, Y.S. Cheng, M. Kchaou, S. Dasari, M.P. Gundupalli, A review of sugarcane biorefinery: from waste to value-added products, Appl. Sci. Eng. Prog. 17 (2024), https://doi.org/10.14416/j.asep.2024.06.004.

[9] Y.S. Fu, H.R. Gao, H. Yu, Q.M. Yang, H. Peng, P. Liu, Y.Q. Li, Z. Hu, R. Zhang, J. Y. Li, Z. Qi, L.Q. Wang, L.C. Peng, Y.T. Wang, Specific lignin and cellulose depolymerization of sugarcane bagasse for maximum bioethanol production under optimal chemical fertilizer pretreatment with hemicellulose retention and liquid recycling, Renew. Energy 200 (2022) 1371–1381, https://doi.org/10.1016/j.renene.2022.10.049.

[10] Z. Hu, Q. Li, Y.Y. Chen, T.Q. Li, Y.M. Wang, R. Zhang, H. Peng, H.L. Wang, Y. T. Wang, J.F. Tang, M. Nauman Aftab, L.C. Peng, Intermittent ultrasound retains cellulases unlock for enhanced cellulosic ethanol with high-porosity biochar for dye adsorption using desirable rice mutant straw, Bioresour. Technol. 369 (2023) 128437, https://doi.org/10.1016/j.biortech.2022.128437.

[11] Y.T. Wang, H.Y. Zhang, Y.N. Li, H. Yu, D. Sun, Y.J. Yang, R. Zhang, L. Yu, F. Ma, M. N. Aftab, L.C. Peng, Y.T. Wang, Effective xylan integration for remodeling biochar uniformity and porosity to enhance chemical elimination and CO_2 adsorption, Int. J. Biol. Macromol. 291 (2025) 138865, https://doi.org/10.1016/j.ijbiomac.2024.138865.

[12] H. Yu, M. Hu, Z. Hu, F. Liu, H.Z. Yu, Q.M. Yang, H.R. Gao, C.B. Xu, M.L. Wang, G. F. Zhang, Y. Wang, T. Xia, L.C. Peng, Y.T. Wang, Insights into pectin dominated enhancements for elimination of toxic Cd and dye coupled with ethanol production in desirable lignocelluloses, Carbohydr. Polym. 286 (2022) 119298, https://doi.org/10.1016/j.carbpol.2022.119298.

[13] S.F. Fu, K.Q. Chen, R. Zhu, W.X. Sun, H. Zou, R.B. Guo, Improved anaerobic digestion performance of *Miscanthus* floridulus by different pretreatment methods and preliminary economic analysis, Energy Convers. Manag. 159 (2018) 121–128, https://doi.org/10.1016/j.enconman.2018.01.014.

[14] D. Tsalagkas, Z. Börcsök, Z. Pásztory, P. Gogate, L. Csóka, Assessment of the papermaking potential of processed *Miscanthus* × giganteus stalks using alkaline pre-treatment and hydrodynamic cavitation for delignification, Ultrason. Sonochem. 72 (2021) 105462, https://doi.org/10.1016/j.ultsonch.2021.105462.

[15] A. Alam, R. Zhang, P. Liu, J. Huang, Y. Wang, Z. Hu, M. Madadi, D. Sun, R. Hu, A. J. Ragauskas, Y. Tu, L. Peng, A finalized determinant for complete lignocellulose enzymatic saccharification potential to maximize bioethanol production in bioenergy *Miscanthus*, Biotechnol. Biofuels Bioprod. 12 (2019), https://doi.org/10.1186/s13068-019-1437-4.

[16] A. Duque, P. Doménech, C. Álvarez, M. Ballesteros, P. Manzanares, Study of the bioprocess conditions to produce bioethanol from barley straw pretreated by combined soda and enzyme-catalyzed extrusion, Renew. Energy 158 (2020) 263–270, https://doi.org/10.1016/j.renene.2020.05.130.

[17] B.Y. He, B. Hao, H.Z. Yu, F. Tu, X.Y. Wei, K. Xiong, Y.J. Zeng, H. Zeng, P. Liu, Y. Y. Tu, Y.T. Wang, H. Kang, L.C. Peng, T. Xia, Double integrating *XYL2* into engineered *Saccharomyces cerevisiae* strains for consistently enhanced bioethanol production by effective xylose and hexose co-consumption of steam-exploded lignocellulose in bioenergy crops, Renew. Energy 186 (2022) 341–349, https://doi.org/10.1016/j.renene.2021.12.103.

[18] G. Kwon, K. Lee, D. Kim, Y. Jeon, U.J. Kim, J. You, Cellulose nanocrystal-coated TEMPO-oxidized cellulose nanofiber films for high performance all-cellulose nanocomposites, J. Hazard. Mater. 398 (2020) 123100, https://doi.org/10.1016/j.jhazmat.2020.123100.

[19] H. Laube, M.T. Reza, Application of biosorbents for ion removal from sodium lactate fermentation broth, J. Environ. Chem. Eng. 4 (2016) 10–19, https://doi.org/10.1016/j.jece.2015.10.044.

[20] J.J. Hou, S.D. Zhang, X.T. Zhang, S.J. Liu, Q.Z. Zhang, Adsorption of ferulic acid from an alkali-pretreated hydrolysate using a new effective adsorbent prepared by a thermal processing method, J. Hazard. Mater. 392 (2020) 122281, https://doi.org/10.1016/j.jhazmat.2020.122281.

[21] M. Wang, Y.X. Wang, J.Y. Liu, H. Yu, P. Liu, Y.J. Yang, D. Sun, H. Kang, Y.T. Wang, J.F. Tang, C.X. Fu, L.C. Peng, Integration of advanced biotechnology for green carbon, Green Carbon 2 (2024) 164–175, https://doi.org/10.1016/j.greenca.2024.02.006.

[22] G.T. Tee, X.Y. Gok, W.F. Yong, Adsorption of pollutants in wastewater via biosorbents, nanoparticles and magnetic biosorbents: a review, Environ. Res. 212 (2022) 113248, https://doi.org/10.1016/j.envres.2022.113248.

[23] D. Heller, D. Einfalt, Wildflower mixtures for bioethanol production - pretreatment and enzymatic hydrolysis, Biomass Bioenergy 141 (2020) 105727, https://doi.org/10.1016/j.biombioe.2020.105727.

[24] J.L. Wu, J. Dong, J.L. Wang, Adsorptive removal of Cu(II) from aqueous solution by fermented sweet sorghum residues as a novel biosorbent, J. Mol. Liq. 367 (2022) 120362, https://doi.org/10.1016/j.molliq.2022.120362.

[25] J. Li, W.J. Zhang, X. Li, T.T. Ye, Y.F. Gan, A. Zhang, H. Chen, G. Xue, Y.N. Liu, Production of lactic acid from thermal pretreated food waste through the fermentation of waste activated sludge: effects of substrate and thermal

pretreatment temperature, Bioresour. Technol. 247 (2018) 890–896, https://doi.org/10.1016/j.biortech.2017.09.186.
[26] L.F. Wang, M.M. Benjamin, A multi-spectral approach to differentiate the effects of adsorbent pretreatments on the characteristics of NOM and membrane fouling, Water Res. 98 (2016) 56–63, https://doi.org/10.1016/j.watres.2016.03.066.
[27] P.R. Yaashikaa, P.S. Kumar, A. Saravanan, D.-V.N. Vo, Advances in biosorbents for removal of environmental pollutants: a review on pretreatment, removal mechanism and future outlook, J. Hazard. Mater. 420 (2021) 126596, https://doi.org/10.1016/j.jhazmat.2021.126596.
[28] W.G. Tian, X.X. Gao, J.M. Zhang, J. Yu, J. Zhang, Cellulose nanosphere: preparation and applications of the novel nanocellulose, Carbohydr. Polym. 277 (2022) 118863, https://doi.org/10.1016/j.carbpol.2021.118863.
[29] Y.L. Betancur, D. López, J. Feng, Z.Y. Du, W.Y. Li, Influence of potassium carbonate catalysis and pre-treatment atmosphere on the textural, structural, and chemical properties of high and low rank coals blended with biomass and their reactivity under conventional and oxy-combustion processes, Energy 220 (2021) 119602, https://doi.org/10.1016/j.energy.2020.119602.
[30] T.Q. Li, H. Peng, B.Y. He, C.Y. Hu, H.Y. Zhang, Y.N. Li, Y.J. Yang, Y.T. Wang, M.M. A. Bakr, M.Z. Zhou, L.C. Peng, H. Kang, Cellulose de-polymerization is selective for bioethanol refinery and multi-functional biochar assembly using brittle stalk of corn mutant, Int. J. Biol. Macromol. 264 (2024) 130448, https://doi.org/10.1016/j.ijbiomac.2024.130448.
[31] J.J. Hou, X.T. Zhang, S.D. Zhang, Q.Z. Zhang, Detoxification of fermentation inhibitors using a waste biomass-based adsorbent of *AEPA250* to enhance bioethanol production: the adsorption analysis and microbial mechanism, Ind. Crop. Prod. 213 (2024) 118436, https://doi.org/10.1016/j.indcrop.2024.118436.
[32] L.L. Cheng, L.Q. Wang, L.Y. Wei, Y. Wu, A. Alam, C.B. Xu, Y.T. Wang, Y.Y. Tu, L. C. Peng, T. Xia, Combined mild chemical pretreatments for complete cadmium release and cellulosic ethanol co-production distinctive in wheat mutant straw, Green Chem. 21 (2019) 3693–3700, https://doi.org/10.1039/C9GC00686A.
[33] N. Xu, W. Zhang, S.F. Ren, F. Liu, C.Q. Zhao, H.F. Liao, Z.D. Xu, J.F. Huang, Q. Li, Y.Y. Tu, B. Yu, Y.T. Wang, J.X. Jiang, J.P. Qin, L.C. Peng, Hemicelluloses negatively affect lignocellulose crystallinity for high biomass digestibility under NaOH and H_2SO_4 pretreatments in *Miscanthus*, Biotechnol. Biofuels Bioprod. 5 (2012) 58, https://doi.org/10.1186/1754-6834-5-58.
[34] M. Madadi, K.L. Zhao, Y.M. Wang, Y.T. Wang, S.W. Tang, T. Xia, N.Z. Jin, Z.J. Xu, G.H. Li, Z. Qi, L.C. Peng, Z.Y. Xiong, Modified lignocellulose and rich starch for complete saccharification to maximize bioethanol in distinct polyploidy potato straw, Carbohydr. Polym. 265 (2021) 118070, https://doi.org/10.1016/j.carbpol.2021.118070.
[35] T.Z. Yuan, J.S. Zeng, B. Wang, Z. Cheng, K.F. Chen, Lignin containing cellulose nanofibers (LCNFs): lignin content-morphology-rheology relationships, Carbohydr. Polym. 254 (2021) 117441, https://doi.org/10.1016/j.carbpol.2020.117441.
[36] N. Bagheri, H.A.J. Al Lawati, J. Hassanzadeh, Simultaneous determination of total phenolic acids and total flavonoids in tea and honey samples using an integrated lab on a chip device, Food Chem. 342 (2021) 128338, https://doi.org/10.1016/j.foodchem.2020.128338.
[37] H.Y. Zhang, Y.T. Wang, H. Peng, B.Y. He, Y.N. Li, H.L. Wang, Z. Hu, H. Yu, Y. T. Wang, M.Z. Zhou, L.C. Peng, M. Wang, Distinct lignocelluloses of plant evolution are optimally selective for complete biomass saccharification and upgrading Cd^{2+}/Pb^{2+} and dye adsorption via desired biosorbent assembly, Bioresour. Technol. 417 (2025) 131856, https://doi.org/10.1016/j.biortech.2024.131856.
[38] Y.M. Sun, M.Z. Li, M.Y. Yang, W.N. Xia, S. Wang, Z.Y. Wang, Y.T. Wang, L.C. Peng, H.Z. Hu, R. Zhang, Engineered cytosolic and chloroplastic UDP-glucose epimerases distinctly modulate xylan interplay for size-tunable cellulose nanocrystals production in Oryza sativa, Carbohydr. Polym. 375 (2026) 124803, https://doi.org/10.1016/j.carbpol.2025.124803.
[39] C.F. Fan, W.Y. Zhang, Y.H. Guo, K. Sun, L.J. Wang, K.M. Luo, Overexpression of *PtoMYB115* improves lignocellulose recalcitrance to enhance biomass digestibility and bioethanol yield by specifically regulating lignin biosynthesis in transgenic poplar, Biotechnol. Biofuels Bioprod. 15 (2022) 119, https://doi.org/10.1186/s13068-022-02218-7.
[40] H. Yu, G.F. Zhang, J.Y. Liu, P. Liu, H. Peng, Z.P. Teng, Y. Li, X.F. Ren, C.X. Fu, J. F. Tang, M. Li, Y.T. Wang, L.Q. Wang, L.C. Peng, A functional cascading of lignin modification via repression of caffeic acid *O*-methyltransferase for bioproduction and anti-oxidation in rice, J. Adv. Res. (2025), https://doi.org/10.1016/j.jare.2025.01.048.
[41] H.L. Wang, S.F. Li, L.M. Wu, W.H. Zou, M.L. Zhang, Y.M. Wang, Z.Y. Lv, P. Chen, P. Liu, Y.J. Yang, L.C. Peng, Y.T. Wang, Semi-overexpressed *OsMYB86L2* specifically enhances cellulose biosynthesis to maximize bioethanol productivity by cascading lignocellulose depolymerization via integrated rapid-physical and recyclable-chemical processes, Green Chem. 27 (2025) 9127–9143, https://doi.org/10.1039/D5GC00658A.
[42] X.Y. Zhang, L.L. Zhang, Y.M. Fan, Z.G. Wang, The case-dependent lignin role in lignocellulose nanofibers preparation and functional application-A review, Green Energy Environ. 8 (2023) 1553–1566, https://doi.org/10.1016/j.gee.2022.09.008.
[43] R. Zhang, Z. Hu, H. Peng, P. Liu, Y.M. Wang, J.Y. Li, J. Lu, Y.T. Wang, T. Xia, L. C. Peng, High density cellulose nanofibril assembly leads to upgraded enzymatic and chemical catalysis of fermentable sugars, cellulose nanocrystals and cellulase production by precisely engineering cellulose synthase complexes, Green Chem. 25 (2023) 1096–1106, https://doi.org/10.1039/D2GC03744K.
[44] A. Isogai, Y. Zhou, Diverse nanocelluloses prepared from TEMPO-oxidized wood cellulose fibers: Nanonetworks, nanofibers, and nanocrystals, Curr. Opin. Solid. St. M. 23 (2019) 101–106, https://doi.org/10.1016/j.cossms.2019.01.001.
[45] Z. Hu, H. Peng, J.Y. Liu, H.Y. Zhang, S.F. Li, H.L. Wang, Z.Y. Lv, Y.M. Wang, D. Sun, J.F. Tang, L.C. Peng, Y.T. Wang, Integrating genetic-engineered cellulose nanofibrils of rice straw with mild chemical treatments for enhanced bioethanol conversion and bioaerogels production, Ind. Crop. Prod. 202 (2023) 117044, https://doi.org/10.1016/j.indcrop.2023.117044.
[46] J.L. Wang, X. Guo, Adsorption isotherm models: classification, physical meaning, application and solving method, Chemosphere 258 (2020) 127279, https://doi.org/10.1016/j.chemosphere.2020.127279.
[47] J.S. Yu, Z.T. Tang, L. Zhu, B. Gao, J. Hong, Y.J. Fang, J.C. Kang, D. Sun, H. Peng, B. Y. He, M.M.A. Bakr, Y.T. Wang, L.C. Peng, H. Yu, Low-temperature $ZnCl_2$ activation of distinct *Miscanthus* lignin as highly-porous biochar assembly for efficient removal of organic dyes, tetracycline and Cr(VI), Ind. Crop. Prod. 240 (2026) 122630, https://doi.org/10.1016/j.indcrop.2026.122630.
[48] Q. Huang, D.W. Hu, M.X. Chen, C.Z. Bao, X. Jin, Sequential removal of aniline and heavy metal ions by jute fiber biosorbents: a practical design of modifying adsorbent with reactive adsorbate, J. Mol. Liq. 285 (2019) 288–298, https://doi.org/10.1016/j.molliq.2019.04.115.
[49] C.F. Fan, G.Y. Wang, L.M. Wu, P. Liu, J.F. Huang, X.H. Jin, G.F. Zhang, Y.P. He, L. C. Peng, K.M. Luo, S.Q. Feng, Distinct cellulose and callose accumulation for enhanced bioethanol production and biotic stress resistance in *OsSUS3* transgenic rice, Carbohydr. Polym. 232 (2020) 115448, https://doi.org/10.1016/j.carbpol.2019.115448.
[50] Y.N. Li, B.Y. He, H.Y. Zhang, J.Y. Liu, S.F. Li, H.L. Wang, H. Peng, Y.T. Wang, J. Dai, Y.T. Wang, L.C. Peng, H. Kang, Enriched extension and cellulose for non-collapse biochar assembly to maximize carbon porosity and dye adsorption with high bioethanol production, Ind. Crop. Prod. 222 (2024) 119924, https://doi.org/10.1016/j.indcrop.2024.119924.